FRONTIERS OF PHYSICS

RESEARCH ARTICLE
Volume 21 / Issue 7 / 072203 / 2026

# Regulation of non-Hermitian couplings in a spontaneous six-wave mixing process

Zhou Feng[1], Rui Zhuang[1], Haitian Tang[1], Sinong Liu[1], Qingyu Chen[1],
Feng Li[1], Kangkang Li[2,†], Yanpeng Zhang[1,‡]

1 Key Laboratory for Physical Electronics and Devices of the Ministry of Education & Shaanxi Key Lab of Information Photonic Technique, Xi'an Jiaotong University, Xi'an 710049, China
2 State Key Laboratory for Artificial Microstructure and Mesoscopic Physics and Frontiers Science Center for Nano-optoelectronics, School of Physics, Peking University, Beijing100871, China
Corresponding authors. E-mail: †kangkangli@pku.edu.cn, ‡ypzhang@mail.xjtu.edu.cn

Received December 27, 2025; accepted April 15, 2026

## ABSTRACT

Non-Hermitian quantum systems — characterized by parity–time symmetry and the emergence of exceptional points — have attracted increasing interest, particularly in light–matter interaction platforms where dissipation and radiative losses play a fundamental role. In this work, we investigate the modulation of coupling states between atomic energy levels during the generation of backward W-state triphotons via a spontaneous six-wave mixing (SSWM) process. By employing tunable external control beams, we realize dynamic modulation from the weak to the strong coupling regime, accompanied by a qualitative transition in triphoton coincidence statistics from anti-bunching to damped Rabi oscillations. Remarkably, the appearance of single exponential decays in the triphoton coincidence count traces marks the onset of an exceptional point in the non-Hermitian system. Furthermore, triphoton correlations in the $\tau_{21}$ and $\tau_{31}$ directions can be independently modulated by selectively tuning of the coupling state via $E_{\mathrm{D1}}$ and $E_{\mathrm{D2}}$, respectively. These results provide a versatile and coherent platform for the one-step generation of backward entangled triphoton states and offer a promising approach to engineering high-dimensional entanglement, with potential applications in quantum communication and quantum information processing.

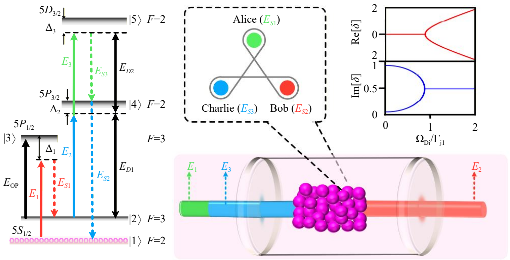

**Keywords** triphotons, quantum optics, non-Hermitian nature, light–matter interaction, temporal correlations

## 1 Introduction

Non-Hermitian quantum systems have emerged as a powerful framework for exploring physical phenomena that are fundamentally inaccessible within conventional Hermitian quantum mechanics [1–3]. Central to this field are exceptional points (EPs) and parity–time (PT) symmetry breaking, which correspond to nontrivial phase transitions characterized by the coalescence of both eigenvalues and their associated eigenstates [4, 5]. In the vicinity of these singularities, non-Hermitian systems exhibit unconventional physical behaviors, including mode coalescence, asymmetric mode conversion, unidirectional transparency, and enhanced sensitivity

---

*Special Topic: Non-Hermitian Physics (Eds.: Peng Xue, Lan Yang & Wu-Ming Liu).

Higher Education Press

https://doi.org/10.15302/frontphys.2026.072203

to external perturbations [6]. These features naturally define the boundary between the weak and the strong coupling regime in dissipative systems and provide new opportunities for controlling light–matter interactions in open quantum environments [7, 8].

Originally proposed in the context of quantum mechanics, PT symmetry has since been realized across a wide range of physical platforms, including birefringent optical media, atomic ensembles, and photomechanical systems [9–11]. Among these, photonic platforms are particularly attractive, as their intrinsic openness — arising from radiative decay, gain, and absorption — naturally gives rise to non-Hermitian dynamics. Consequently, photonic and atomic systems have become versatile testbeds for investigating EP physics and non-Hermitian light–matter interactions [12–14]. More recently, these concepts have been extended into the quantum regime, where EPs have been shown to significantly influence quantum state evolution, enhance sensing performance, and enable new approaches for controlling open-system dynamics [13, 15–18].

Beyond classical wave phenomena, non-Hermitian physics has attracted growing attention in nonlinear quantum optical systems, where the interplay between dissipative coupling and coherent light–matter interactions can strongly modify quantum correlations and photon statistics [19, 20]. In particular, nonlinear optical processes in atomic ensembles [21], such as spontaneous four-wave mixing (SFWM) and spontaneous six-wave mixing (SSWM) [22], provide powerful platforms for generating nonclassical light fields including biphotons, triphotons, and higher-order multiphoton states [23, 24]. These systems allow precise control over the spectral, temporal, and statistical properties of correlated photons through mechanisms such as electromagnetically induced transparency (EIT) [25, 26], slow-light effects, and coherent population manipulation [27, 28].

Recent theoretical and experimental studies have indicated that non-Hermitian coupling structures can fundamentally modify the effective coupling between atomic energy levels, leading to transitions across distinct coupling regimes [29–31]. In this context, exceptional points can manifest through characteristic signatures in correlation functions, reflecting underlying changes in the eigenmode structure of the open quantum system. Therefore, integrating non-Hermitian physics with nonlinear quantum optical processes provides a promising route for engineering multiphoton quantum states and tailoring their temporal correlations [32]. While the nonlinear scaling behavior of multiphoton generation has been extensively investigated [33], the non-Hermitian control of multiphoton temporal correlations under fixed generation conditions remains largely unexplored.

In this work, we demonstrate dynamic control of energy-level coupling states during the generation of *W*-state entangled triphotons via a spontaneous six-wave mixing (SSWM) process in a naturally non-Hermitian atomic system. By precisely tuning the Rabi frequency of two external control beams, $E_{\mathrm{D}1}$ and $E_{\mathrm{D}2}$, we realize a dynamic modulation spanning the weak- to strong-coupling regimes, accompanied by a pronounced transition in the triphoton coincidence counting — from anti-bunching behavior to damped Rabi oscillations. The emergence of single-exponential decays in the coincidence counts provides evidence of the presence of exceptional points in the system. Furthermore, we demonstrate that triphoton correlations along the $\tau_{21}$ and $\tau_{31}$ directions can be independently modulated by selectively tuning the coupling states via $E_{\mathrm{D}1}$ and $E_{\mathrm{D}2}$, respectively. Our results establish a novel approach for engineering controllable non-Hermitian quantum processes without relying on artificial photonic structures, thereby opening new avenues for high-dimensional quantum control and entanglement manipulation based on non-Hermitian light–matter interactions.

## 2 Method

As portrayed in Fig. 1, our objective is to generate narrowband *W*-state entangled triphotons from a 7-cm-long $^{85}$Rb vapor cell with a five-level configuration. This is achieved through the interaction between an atomic ensemble and three counter-propagating continuous-wave laser beams: a weak pump beam ($E_1$: $\omega_1$, $\kappa_1$) and two strong coupling beams ($E_2$: $\omega_2$, $\kappa_2$; $E_3$: $\omega_3$, $\kappa_3$). Through a Doppler-broadened spontaneous six-wave mixing (SSWM) process, backward-propagating photon triplets ($E_{Sj}$: $\omega_{Sj}$, $\kappa_{Sj}$ with $j = 1, 2, 3$) are emitted. This nonlinear process satisfies both energy conservation ($\omega_1+\omega_2+\omega_3=\omega_{S1}+\omega_{S2}+\omega_{S3}$) and phase-matching conditions ($k_1+k_2+k_3=k_{S1}+k_{S2}+k_{S3}$), enabling the generation of time-energy entangled *W*-state triphotons. The three generated photons are labeled as Alice ($E_{S1}$), Bob ($E_{S2}$), and Charlie ($E_{S3}$), as depicted in Fig. 1(a). In this entangled state, the properties of each photon are intrinsically linked to those of the other two, reflecting the nonlocal correlations inherent in the *W*-state entanglement [34, 35].

In our scheme, time-energy entangled triphotons ($E_{S1}$, $E_{S2}$ and $E_{S3}$) are generated via the SSWM process in a five-level rubidium atomic system, as illustrated in Fig. 1(b). Five relevant energy levels are $|1\rangle$ ($5S_{1/2}$ F $=2$), $|2\rangle$ ($5S_{1/2}$ F $=3$), $|3\rangle$ ($5P_{1/2}$ F $=2$), $|4\rangle$ ($5P_{3/2}$ F $=3$), and $|5\rangle$ ($5D_{3/2}$ F $=2$) in $^{85}$Rb. $E_1$ connects the transition $|1\rangle \longrightarrow |3\rangle$ with a large red frequency detuning, which can retard the atomic noise and force the atomic population to remain in the ground state. Others two strong coupling beams $E_2$ and $E_3$ couple $|2\rangle \longrightarrow |4\rangle$ and $|4\rangle \longrightarrow |5\rangle$, respectively. Furthermore, two external

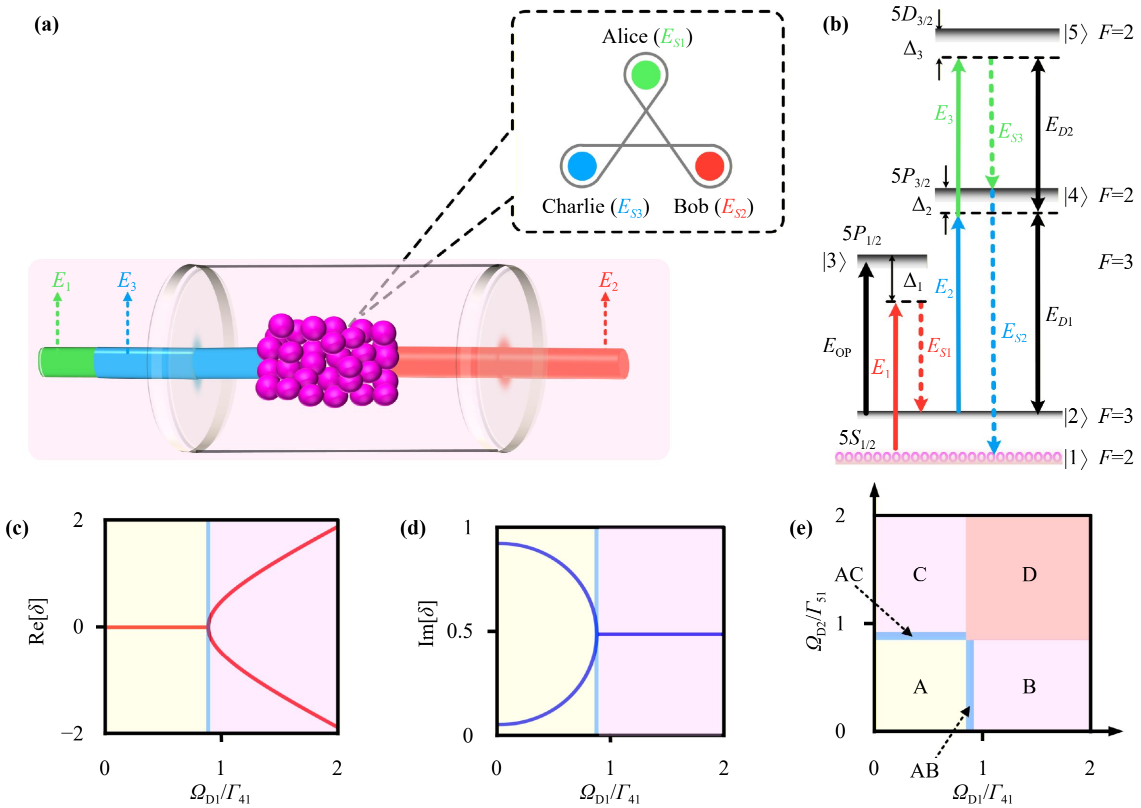

**Fig. 1** Schematic illustration of the $W$-triphoton generation via the SSWM process. **(a)** Schematic of triphoton generation in a hot atomic vapor cell. **(b)** Energy level diagram for the SSWM process in a 5-level system of $^{85}$Rb atoms. **(c, d)** Eigenvalue surfaces diagram for the real part and imaginary parts, respectively, as functions of $\Omega_{\mathrm{D1}}/\Gamma_{41}$. **(e)** Phase diagram illustrating the different coupling regimes — weak, strong, and EP — as functions of the normalized parameters $\Omega_{\mathrm{D1}}/\Gamma_{41}$ and $\Omega_{\mathrm{D2}}/\Gamma_{51}$. Each colored region corresponds to a distinct eigenstate configuration, where the transitions in (c) and (d) map onto regimes A, AB and B in (e).

control beams, $E_{\mathrm{D1}}$ and $E_{\mathrm{D2}}$, are applied to couple the energy levels $|2\rangle$ to $|4\rangle$ and $|4\rangle$ to $|5\rangle$, respectively, enabling precise control over the energy level couple state in the process. To eliminate residual population in level $|2\rangle$ and suppress noise from spontaneous Raman scattering, a strong on-resonance optical pumping field $E_{OP}$ is applied to the $|2\rangle \longrightarrow |3\rangle$ transition [36].

To compute the resultant triphoton state arising from the SSWM process, we analyze the triphoton coincidence counting rate across various energy level configurations at the output surfaces of the medium. Physically, the interaction Hamiltonian of the triphoton generation process is defined as (neglecting the reflections from surfaces and employing the rotating-wave approximation) [37–39]:

$$H = \varepsilon_0 \int_V \mathrm{d}^3 r \chi^{(5)} E_1 E_2 E_3 E_{S3}^{(-)} E_{S2}^{(-)} E_{S1}^{(-)} + H.c, \tag{1}$$

where $\chi^{(5)}$ represents the fifth-order Doppler-broadened nonlinear susceptibility, $V$ is the interaction volume illuminated by the input fields and $H.c$ is the Hermitian conjugate [40]. The state vector of the triphotons can be derived using first-order perturbation theory in the Schrödinger picture and can be formulated as follows [38]:

$$|\psi\rangle = \iiint \mathrm{d}\omega_{S1}\mathrm{d}\omega_{S2}\mathrm{d}\omega_{S3}\chi^{(5)}\Phi\left(\frac{\Delta KL}{2}\right)\delta(\Delta\omega)\,|\omega_{S1},\omega_{S2},\omega_{S3}\rangle. \tag{2}$$

Here, $\Delta\omega = \omega_{S1} - \omega_1 + \omega_{S2} - \omega_2 + \omega_{S3} - \omega_3$; $\Phi(\Delta KL/2) = \mathrm{sinc}\,(\Delta kL/2)\,\mathrm{e}^{-\mathrm{i}\Delta kL/2}$ is the phase-mismatch longitudinal function which ascribes the triphoton natural spectral width arising from their different group velocities; $L$ is the interaction length; $\Delta k = \Delta\boldsymbol{k}\cdot\hat{\boldsymbol{z}}$ is the phase mismatch; Dirac function ($\delta$) is derived from the time integral in the steady-state approximation, ensuring the energy conservation in the SSWM process [41].

Consequently, the fifth-order Doppler-broadened nonlinear susceptibility $\chi^{(5)}$ in the SSWM process can be identified as

$$\chi^{(5)}\left(\delta_2,\delta_3\right)=\int \mathrm{d}\nu \frac{2f\left(\nu\right)N\mathrm{i}\mu_{13}\mu_{23}\mu_{24}\mu_{45}^2\mu_{14}}{\varepsilon_0\hbar^5\left[\begin{array}{c}\left(\Gamma_{31}+\mathrm{i}\Delta_{B1}\right)\left(\Gamma_{21}+\mathrm{i}W_{\mathrm{D}-}\delta_2+\mathrm{i}W_{\mathrm{D}+}\delta_3\right)\left(\Gamma_{41}+\mathrm{i}\Delta_{\mathrm{B2}}+\mathrm{i}W_{\mathrm{D}-}\delta_2+\mathrm{i}W_{\mathrm{D}+}\delta_3\right)\\ \left(\Gamma_{51}+\mathrm{i}\Delta_{\mathrm{B2}}+\mathrm{i}\Delta_{\mathrm{B3}}+\mathrm{i}W_{\mathrm{D}-}\delta_2+\mathrm{i}W_{\mathrm{D}+}\delta_3\right)\left(\Gamma_{41}+\mathrm{i}\Delta_{\mathrm{B2}}+\mathrm{i}W_{\mathrm{D}-}\delta_2+d_1+d_2\right)\end{array}\right]}. \tag{3}$$

Here $f\left(\nu\right)=\sqrt{\frac{m_{\mathrm{Rb}}}{2\pi k_{\mathrm{B}}T}}\exp\left(-\frac{m_{\mathrm{Rb}}v^2}{2k_{\mathrm{B}}T}\right)$ is the Maxwell–Boltzmann velocity distribution of the Rb atoms in the thermal motion, where $m_{\mathrm{Rb}}$ is the mass of the Rb atom, $k_{\mathrm{B}}$ is the Boltzmann constant, $T$ is the vapor temperature, and $v$ is the atomic kinetic velocity; $N$ is atomic density, $\mu_{ij}$ ($i$, $j$ = 1, 2, 3, 4, 5) refers to the electric dipole matrix elements for the atomic transition $|i\rangle\rightarrow|j\rangle$, $\Gamma_{ij}=\left(\Gamma_i+\Gamma_j\right)/2$ is the decoherence rate between levels $|i\rangle$ and $|j\rangle$; $\Delta_{Bi}=\Delta_i+v\omega_{ij}/c$ with frequency detuning $\Delta_i=\omega_{ij}-\omega_i$, and $\omega_{ij}$ being the frequency between levels $|i\rangle$ and $|j\rangle$; $W_{\mathrm{D}\pm}=1\pm v/c$ accounts for the first-order Doppler shift which depends on atomic velocity with $c$ the speed of light in vacuum, $c$ is the speed of light in the vacuum; $\Omega_{\mathrm{D1}}$ and $\Omega_{\mathrm{D2}}$ are the Rabi frequency of $E_{\mathrm{D1}}$ and $E_{\mathrm{D2}}$; $\delta_i$ represents the deviations around the corresponding central frequency $\varpi_{Si}$ of generated photons that is $\omega_{Si}=\varpi_{Si}+\delta_i$ ($i$ = 1, 2) where $|\delta_i|\ll\varpi_{Si}$. Furthermore, it is essential to recognize that, due to the energy conservation in SSWM, the generation of these two photons is contingent upon the detection of the output $E_{S1}$ photon at the frequency $\omega_{S1}=\omega_1+\omega_2+\omega_3-\omega_{S2}-\omega_{S3}$. This necessitates that the spectral distributions of the entangled triphoton state must satisfy the condition $\delta_1+\delta_2+\delta_i=0$ [41].

To enhance the fifth-order nonlinear interaction, a length of $L$ = 7 cm $^{85}$Rb vapor cell is heated to 80 °C using a resistive heating tape [38]. At this temperature, the Doppler broadening is estimated to be approximately $\Delta_{\mathrm{D}}$ = 555 MHz, which is several orders of magnitude larger than the Rb natural linewidth [38]. The atomic density is calculated to be $N = 1.2\times10^{11}$ cm$^{-3}$, based on $N=P/\left(k_{\mathrm{B}}T\right)$, where $P$ is the saturated vapor pressure and $k_{\mathrm{B}}$ is the Boltzmann constant. The optical depth (OD), defined as $OD=N\sigma_{41}L$, has a value of 4.6, where $\sigma_{41}=3\pi N\Gamma_{41}c^2/\left(2\Delta_{\mathrm{D}}\omega_{41}^2\right)$ is the on-resonance absorption cross-section for the transition $|1\rangle\longrightarrow|4\rangle$ [36]. When the temperature is increased to 115 °C, the OD rises to 45.7.

A coupled atomic energy-level system, such as the transition $|2\rangle\longrightarrow|4\rangle$ driven by a coupling laser field with Rabi frequency $\Omega_{\mathrm{D1}}$ and detuning $\Delta_{\mathrm{D1}}$ [Fig. 1(b)], can be effectively described by a non-Hermitian Hamiltonian. For the control field $E_{\mathrm{D1}}$, which couples the energy levels $|2\rangle$ and $|4\rangle$, the effective Hamiltonian is given by [3, 18]

$$H_{nH-D1}=\left(\begin{array}{cc}-\mathrm{i}\Gamma_{21} & \Omega_{\mathrm{D1}}\\ \Omega_{\mathrm{D1}} & \Delta_{\mathrm{D1}}-\mathrm{i}\Gamma_{41}\end{array}\right), \tag{4}$$

where $\Gamma_{ij}=\left(\Gamma_i+\Gamma_j\right)/2$ is decoherence rate between $|i\rangle$ and $|j\rangle$. $\Gamma_i$ represents the decay rate of the $|i\rangle$. $\Omega_{\mathrm{D1}}$ is the Rabi frequency induced by the optical field $E_{\mathrm{D1}}$, while $\Delta_{\mathrm{D1}}$ is corresponding to the associated detuning. Eq. (4) is a typical non-Hermitian Hamiltonian containing coupling and dissipative terms. The corresponding eigenvalues are expressed as

$$\delta_{D1\pm}=\Delta_{\mathrm{D1}}/2-\mathrm{i}\Gamma_{effa}\pm\sqrt{\Omega_{\mathrm{D1}}^2+\left(\Delta_{\mathrm{D1}}/2-\mathrm{i}\Gamma_{diffa}\right)^2}, \tag{5}$$

where $\Gamma_{effa}=\left(\Gamma_{21}+\Gamma_{41}\right)/2$ is the effective decoherence rate defined as the average value of the holistic loss factor of system, and $\Gamma_{diffa}=\left(\Gamma_{21}-\Gamma_{41}\right)/2$ is the difference between the two decoherence rates. At zero detuning, the complex eigenvalues of $H_{nH-\mathrm{D1}}$ have different resonant components when $\Omega_{\mathrm{D1}}>\Gamma_{diffa}$, indicating that the system operates in the strong coupling regime. Passing the EP at $\Omega_{\mathrm{D1}}=\Gamma_{diffa}$, where the imaginary components for the two resonant eigenstates coalesce, it enters the weak coupling regime when $\Omega_{\mathrm{D1}}<\Gamma_{diffa}$.

Similar to the two-level non-Hermitian subsystem formed by coupling energy levels $|2\rangle$ and $|4\rangle$ via $E_{\mathrm{D1}}$, another two-level non-Hermitian system can be constructed through the coupling between energy levels $|4\rangle$ and $|5\rangle$ driven by $E_{\mathrm{D2}}$. In this configuration, the corresponding Rabi frequency and detuning are denoted by $\Omega_{\mathrm{D2}}$ and $\Delta_{\mathrm{D2}}$, respectively. Unlike the eigenequation in Eq. (5), the eigenvalue equation is $\delta_{\mathrm{D2}\pm}=\Delta_{\mathrm{D2}}/2-\mathrm{i}\Gamma_{effb}\pm\sqrt{\Omega_{\mathrm{D2}}^2+\left(\Delta_{\mathrm{D2}}/2-\mathrm{i}\Gamma_{diffb}\right)^2}$, where $\Gamma_{effb}=\left(\Gamma_{41}+\Gamma_{51}\right)/2$ and $\Gamma_{diffb}=\left(\Gamma_{41}-\Gamma_{51}\right)/2$. The complex eigenvalues reveal distinct resonant components when $\Omega_{\mathrm{D2}}>\Gamma_{diffb}$, indicating that the system operates in the strong-coupling regime. The imaginary parts of the two eigenstates coalesce at the EP when $\Omega_{\mathrm{D2}}=\Gamma_{diffb}$ marking the transition between distinct dynamical phases. Conversely, when $\Omega_{\mathrm{D2}}<\Gamma_{diffb}$, the system enters the weak-coupling regime, where dissipation dominates the dynamics and coherent mode splitting vanishes.

Based on the above eigenvalue formulations of non-Hermitian physics and the experimental configuration employed in this study, we simulated the evolution of the system's eigenvalues changing with external control beam. Figures 1(c) and (d) illustrate the variations in the real and imaginary parts of the system's eigenvalues as functions of $\Omega_{\mathrm{D1}}/\Gamma_{41}$. As $\Omega_{\mathrm{D1}}/\Gamma_{41}$ increases, significant changes in both the real and imaginary parts of the eigenvalues are exhibited. To further analyze these results, we categorized the eigenvalue surfaces diagram into distinct regimes based on changes in eigenvalue (Fig. 1 and Fig. S3). Furthermore, we constructed a two-dimensional phase diagram to map these eigenstates, as illustrated in Fig. 1(e) [1, 7]. In this phase diagram, each colored regime represents a distinct eigenstate [42]. This comprehensive analysis provides a clear visualization of the system's non-Hermitian dynamics and its dependence on the control parameters $\varOmega_{\mathrm{D1}}/\varGamma_{41}$ and $\varOmega_{\mathrm{D2}}/\varGamma_{51}$.

Furthermore, by analyzing the coincidence counting rate of the triphoton state, its non-classical behavior can be demonstrated by verifying a violation of the Cauchy–Schwarz inequality. The correlation properties of the triphoton can be analyzed using the following inequality:

$$\frac{\left[g^{(3)}\left(\tau_{21},\tau_{31}\right)\right]^2}{\left[g_{S1}^{(2)}\right]\left[g_{S2}^{(2)}\right]\left[g_{S3}^{(2)}\right]} \le 1, \tag{6}$$

where $g^{(3)}\left(\tau_{21},\tau_{31}\right)$ is the normalized third-order cross-correlations function, $g_{Si}^{(2)}$ $(i = 1,\ 2,\ 3)$ represents the normalized second-order autocorrelations of the emitted photons $E_{Si}$. The third-order cross-correlation function $g^{(3)}\left(\tau_{21},\tau_{31}\right)$, is obtained by normalizing the triphoton coincidence counts to the flat background of accidental coincidence counts, while $g_{Si}^{(2)}$ $(i = 1,\ 2,\ 3)$ can be measured using a fiber beam splitter. Therefore, if the calculated from Eq. (5) is larger than 1, it suggests strong correlation in the triphoton state, providing evidence of its non-classical behavior.

The experimental configuration for triphoton generation via SSWM is illustrated in Fig. 2(a). The process takes place in a paraffin-coated $^{85}$Rb vapor cell with a length of $L = 7$ cm. Three continuous-wave laser beams — $E_1$, $E_2$ and $E_3$ — are independently generated by external cavity diode lasers (LD1, LD2, and LD3). $E_1$ (frequency $\omega_1$, wave vector $k_1$, Rabi frequency $\varOmega_1$) is horizontally polarized. $E_2$ $(\omega_2,\ k_2,\ \varOmega_2)$ is vertically polarized and propagates counter to $E_1$, while $E_3$ $(\omega_3,\ k_3,\ \varOmega_3)$ is also vertically polarized and propagates codirectionally with $E_1$. By carefully aligning the beams to satisfy the phase-matching conditions $(k_1 + k_2 + k_3 = k_{S1} + k_{S2} + k_{S3})$ and energy conservation $(\omega_1 + \omega_2 + \omega_3 = \omega_{S1} + \omega_{S2} + \omega_{S3})$, triphoton $E_{S1}$, $E_{S2}$ and $E_{S3}$ are spontaneously generated. To regulate the coupling dynamics and probe non-Hermitian behavior, two additional control beams $E_{\mathrm{D1}}$ and $E_{\mathrm{D2}}$ are introduced into the vapor cell at large crossing angles relative to the primary SSWM driving fields ($E_1$, $E_2$ and $E_3$). This configuration suppresses their direct involvement in the SSWM phase-matching process, allowing them to primarily engineer the effective non-Hermitian coupling between the relevant atomic levels. In addition, a strong on-resonance optical pumping beam $E_{OP}$ (LD4, $\omega_{OP}$, $\lambda = 795$ nm) is applied to the $|2\rangle \longrightarrow |3\rangle$ transition to depopulate residual atoms in $|2\rangle$ and suppress unwanted background from spontaneous Raman scattering [36].

During the detection process, the spontaneously generated entangled triphotons are coupled into three single-mode fibers (SF) with a 4° angle relative to the excitation beams. Each photon passes through a narrowband optical filter (NF) followed by a custom-designed Fabry–Pérot cavity filter (FP) with a bandwidth of approximately 600 MHz. The combined filtering system provides a transmission efficiency of about 80% and an extinction ratio of 60 dB, efficiently suppressing background noise while isolating the desired spectral components. Finally, the filtered photons are detected using a single-photon counting module (SPCM), with a fiber coupling efficiency of approximately 70% and a detector quantum efficiency of 40%. Despite these filtering measures, residual background noise remains, contributing to background counts in the triphoton coincidence measurements [43]. The photon arrival times are recorded by a time-tagging module (IDQ-ID900) and subsequently processed via a computer.

Figures 2(b)–(g) illustrate energy-level diagrams corresponding to various modulation regimes of triphoton generation in the SSWM process. Figures 2(b)–(d) focus on the coupling dynamics between $|2\rangle$ and $|4\rangle$, directly influencing the generation pathway of $E_{S2}$. In Fig. 2(b), $|2\rangle \longleftrightarrow |4\rangle$ operate in the weak coupling regime [region A in Fig. 1(e)]. The low-intensity coupling fields result in minimal energy-level perturbation, with $E_{S2}$ exhibiting one resonant channel (dashed lines) and two absorptive channels (dotted curves). In this regime, the generation of $E_{S2}$ is predominantly governed by the linear susceptibility, with $\Delta\omega_{g2} \ll [|\varOmega_{e2}|, \varGamma_{eff2}]$. Figure 2(c) represents an intermediate regime [AB in Fig. 1(e)], where the $|2\rangle \longleftrightarrow |4\rangle$ transition operates at an EP. In this case, the generation of $E_{S2}$ exhibits one resonant and one absorptive channel. In Fig. 2(d), the $|2\rangle \longleftrightarrow |4\rangle$ transition enters the strong coupling regime (region B), leading to dressed-state splitting of $|4\rangle$ into two components separated by $\hbar\varOmega_{e1}$. In this regime, $\Delta\omega_{g2} \gg [|\varOmega_{e2}|, \varGamma_{eff2}]$, and the triphoton correlation is determined by the coexistence of $\chi$ and $\chi^{(5)}$, with $E_{S2}$ exhibiting two resonant and one absorptive channel.

Figures 2(e)–(g) present the corresponding modulation of the coupling state between $|4\rangle$ and $|5\rangle$, which determine the generation pathways of $E_{S3}$. In Fig. 2(e), $|4\rangle \longleftrightarrow |5\rangle$ operate in the weak coupling regime [region A in Fig. 1(e)], with $E_{S3}$ exhibiting one resonant channel (dashed lines) and two absorptive channels (dotted curves). In this regime, the generation of $E_{S3}$ is predominantly governed by the linear susceptibility, with $\Delta\omega_{g3} \ll [|\varOmega_{e3}|, \varGamma_{eff3}]$. In Fig. 2(f), the system corresponds to regime AC, with $|4\rangle \longleftrightarrow |5\rangle$ at an EP. $E_{S3}$ exhibits one resonant and one absorptive channel, governed primarily by $\Delta\omega_{g3} < [|\varOmega_{e3}|, \varGamma_{eff3}]$. In Fig. 2(g), the $|4\rangle \longleftrightarrow |5\rangle$ transition enters the strong coupling regime (region C), leading to dressed-state splitting of $|5\rangle$ into two components separated by $\hbar\varOmega_{e2}$. In this regime, $\Delta\omega_{g3} \gg [|\varOmega_{e3}|, \varGamma_{eff3}]$, and the triphoton correlation is dominantly governed by the dressed-state nonlinear susceptibility $\chi^{(5)}$. These results comprehensively illustrate the interplay between exceptional points, dressed states,

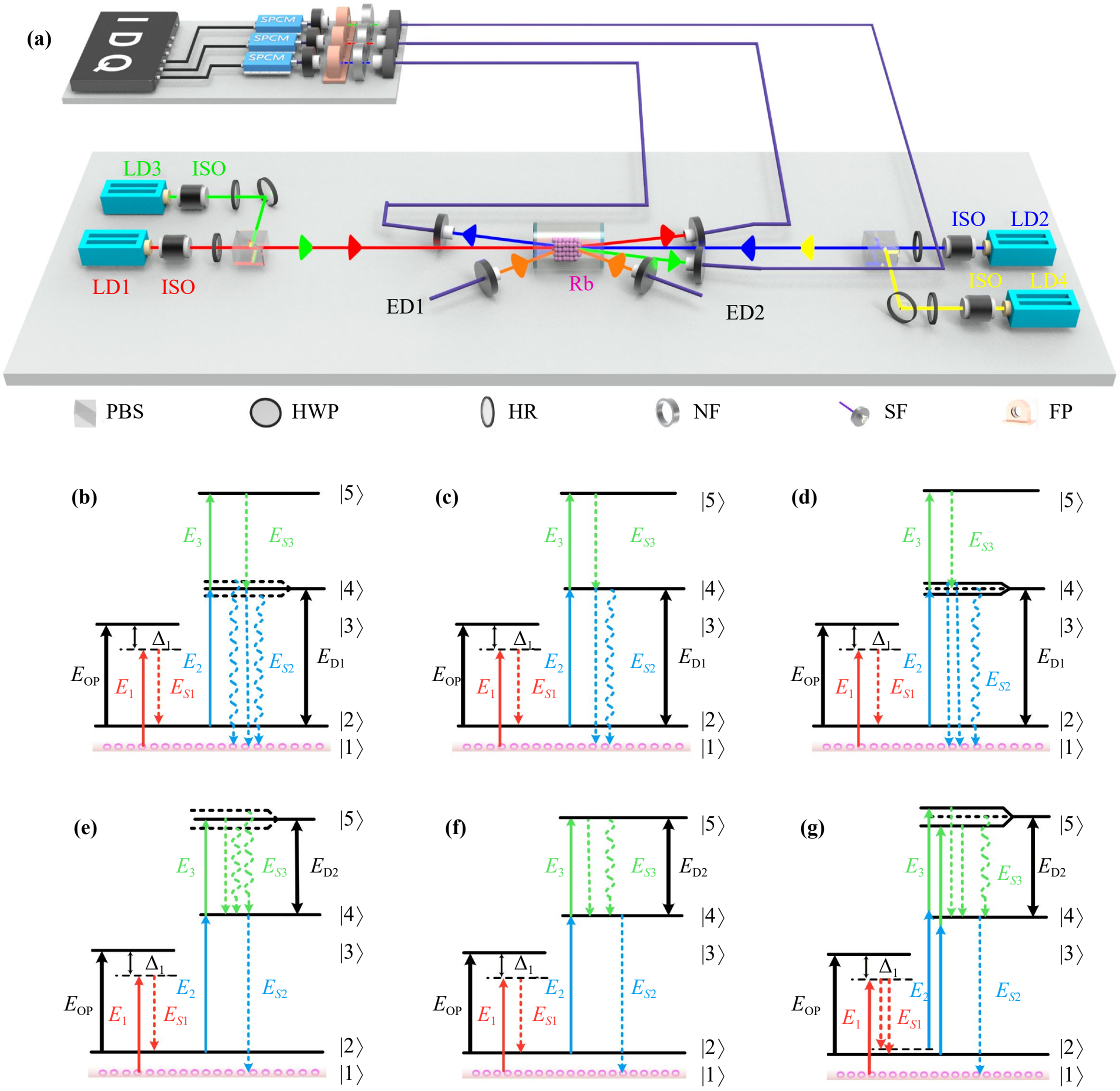

**Fig. 2** Experimental setup and energy-level configurations for *W*-state triphoton generation via the SSWM process. **(a)** Schematic of the experimental setup. Three continuous-wave laser beams — $E_1$ (795 nm), $E_2$ (780 nm), and $E_3$ (776 nm) — are derived from external cavity diode lasers (LD1–LD3), each passing through optical isolators (ISO) to prevent back reflections. The beams are spatially and polarization-aligned using half-wave plates (HWP), high-reflectivity mirrors (HR), and a polarization beam splitter (PBS) to satisfy phase-matching conditions of SSWM within the paraffin-coated $^{85}$Rb vapor cell. Through the Doppler-broadened SSWM process, backward-propagating triphotons are emitted and collected at a 4° angle into single-mode fibers (SF) to spatially separate them from the incident beams. The collected photons are filtered by narrowband optical filters (NF) and custom-designed Fabry–Pérot (FP) etalons to suppress the scattered photons. Triphotons are detected by three single-photon counting modules (SPCMs) positioned equidistantly from the vapor cell center. The coincidence events are registered using a time-to-digital converter with a resolution of 813 fs. **(b–g)** Schematic diagram of the energy-level state involved in the SSWM process under different coupling states, modified by varying the Rabi frequency of $E_{D1}$ or $E_{D2}$, where the straight line represents the generation channel, the curve line is the attenuation channel.

and multiphoton correlations in the SSWM process, providing a framework for manipulating triphoton quantum states via controlled energy-level coupling.

## 3 Results

In this experiment, we investigate the temporal correlation properties of triphotons generated via the SSWM process, focusing on how these correlations evolve under different coupling regimes between two pairs of energy levels. Compared with our previous work based on biphotons generated via SFWM, the present study extends the non-Hermitian control scheme to a higher-order nonlinear interaction, enabling the generation and manipulation of time–energy–entangled *W*-state tripho-

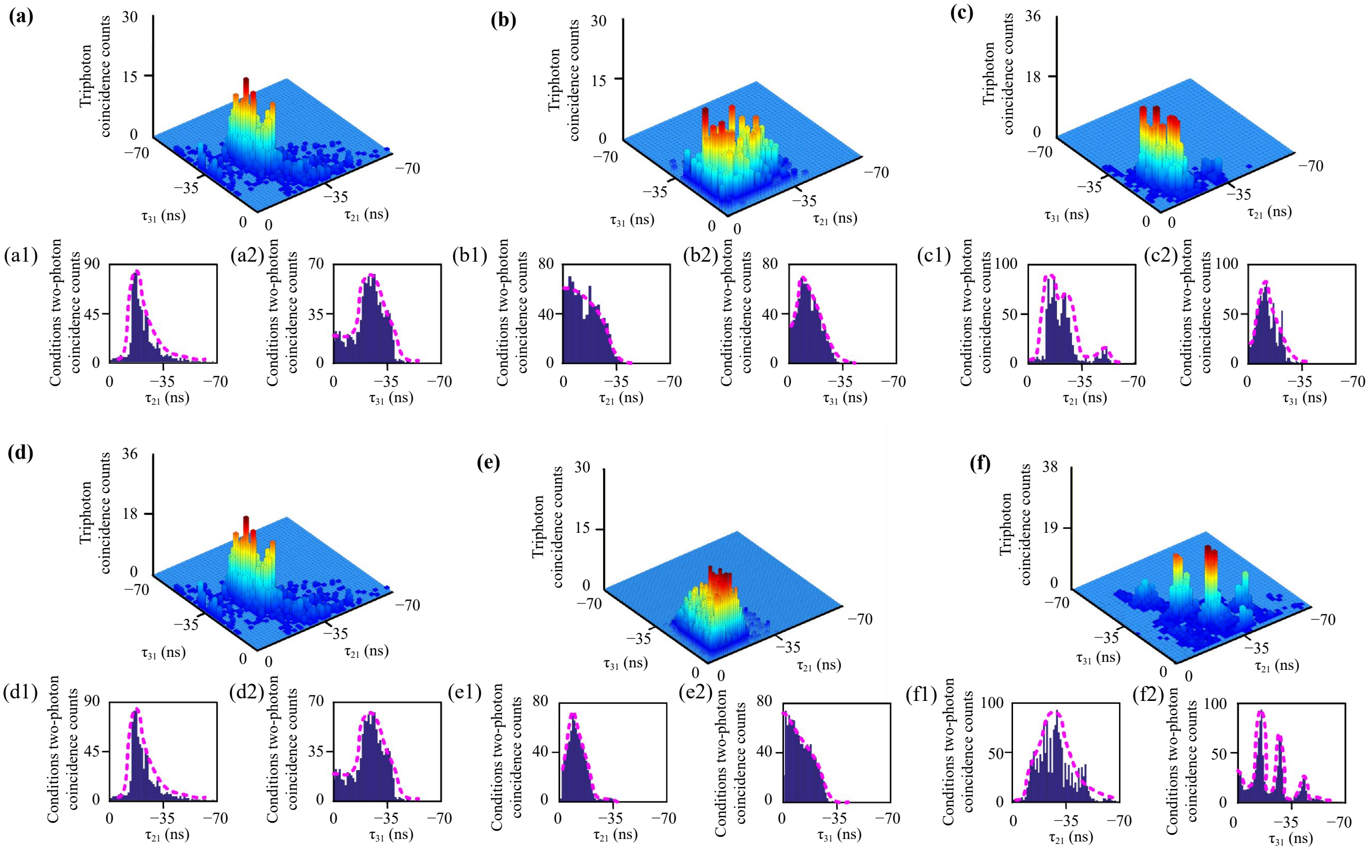

**Fig. 3** Triphoton coincidence counting measurements collected over 1 hour with a time bin of 0.25 ns. The upper panels **(a–f)** present three-dimensional histograms of triphoton coincidence counts plotted in the ($\tau_{21}$, $\tau_{31}$) parameter space. The corresponding lower subfigures (a1–f1) and (a2–f2) display the conditional two-photon coincidence counts for (a–f) in $\tau_{21}$ and $\tau_{31}$ directions, respectively. (a) Triphoton coincidence measurement with $\Omega_{\rm D1} = 5$ MHz and $\Omega_{\rm D2} = 0$ MHz. (b) and (c) Triphoton collected under identical conditions as (a), except that $\Omega_{\rm D1} = 15.9$ MHz and $\Omega_{\rm D1} = 37.9$ MHz, respectively. (d) Triphoton coincidence measurement with $\Omega_{\rm D1} = 0$ MHz and $\Omega_{\rm D2} = 3.50$ MHz. (e, f) Triphoton collected under identical conditions as (d), except that $\Omega_{\rm D1} = 26.4$ MHz and $\Omega_{\rm D1} = 39.5$ MHz, respectively.

tons in a five-level atomic system. The coupling states are precisely tuned by adjusting the Rabi frequencies of $E_{\rm D1}$ and $E_{\rm D2}$. The triphotons, labeled $E_{S1}$, $E_{S2}$, and $E_{S3}$, are generated through the absorption of one pump photon ($E_1$) and two coupling photons ($E_2$ and $E_3$). $E_1$ operates with a large red frequency detuning of $\Delta_1 = 2.36$ GHz and a power of $P_1 = 6$ mw; $E_2$ works with a power of $P_2 = 8$ mw and a detuning of $\Delta_2 = 200$ MHz; $E_3$ has a power of $P_3 = 10$ mw and a detuning of $\Delta_3 = 50$ MHz. The triphoton signals are accumulated over an acquisition time of one hour with a temporal bin width of 0.25 ns. Within a coincidence window of 120 ns, the detection of an $E_{S1}$-photon as triggered the start of a coincidence event that ended with the detection of subsequent $E_{S2}$- and $E_{S3}$-photons. The coincidence counting measurements of triphoton display as the histogram in the parameter space ($\tau_{21}$, $\tau_{31}$), where $\tau_{21} = \tau_2$–$\tau_1$ and $\tau_{31} = \tau_3$–$\tau_1$ are respectively the relative time delays with $\tau_{\rm j}$ being the triggering time of the SPCM*j*.

Figure 3 presents the triphoton coincidence counting under different coupling states achieved by varying the Rabi frequency of $E_{\rm D1}$ and $E_{\rm D2}$. In Fig. 3(a), the Rabi frequency of $E_{\rm D1}$ and $E_{\rm D2}$ are $\Omega_{\rm D1} = 5$ MHz and $\Omega_{\rm D2} = 0$ MHz. The triphoton coincidence counting exhibits anti-bunch exponential decay along both the $\tau_{21}$ and $\tau_{31}$ directions, with peak counts located at $\tau_{21} = -16$ ns and $\tau_{31} = -25$ ns. According to the system's eigenvalue analysis, $\delta_{\rm D1}$ corresponds to weak coupling regimes where $\Omega_{\rm D1} < \Gamma_{diffa}$, resulting in one real and two imaginary components. The associated energy-level configuration corresponds to Fig. 2(b), where the coupling pathways of the generation of $E_{S2}$ is in the weak state. In Fig. 3(b), increasing $\Omega_{\rm D1}$ to 15.9 MHz drives the $|2\rangle \longleftrightarrow |4\rangle$ transition to an exceptional point (EP). The coincidence histogram reveals a single exponential decay along the $\tau_{21}$ and an anti-bunching decay along $\tau_{31}$, indicating that $\delta_{\rm D1}$ has coalesced into one real and one imaginary part (at EP, $\Omega_{\rm D1} = \Gamma_{diffa}$). This state corresponds to the EP regime illustrated in Fig. 2(c), where the quantum state associated with $E_{S2}$ is significantly modified.

In Fig. 3(c), further increasing $\Omega_{\rm D1}$ to 37.9 MHz drives

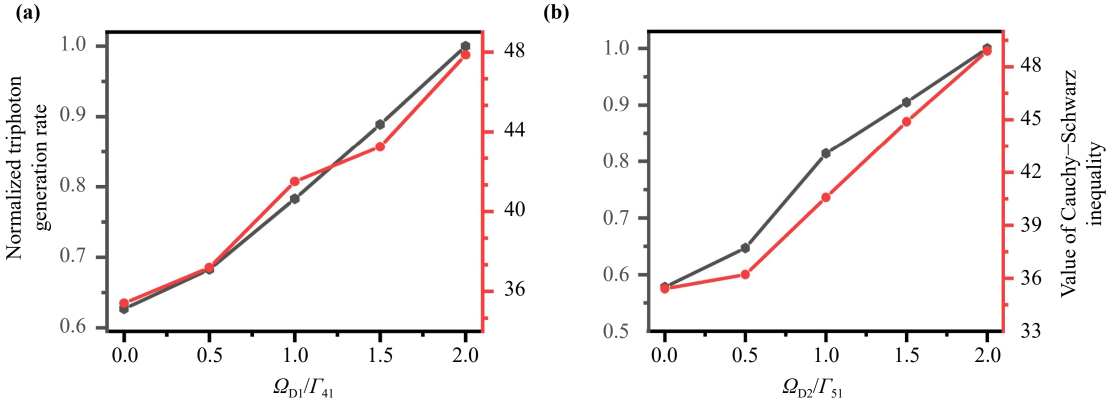

**Fig. 4** Ttriphoton generation rates and Cauchy-Schwarz inequality violation under different conditions. **(a)** Measured triphoton generation rates and the Cauchy–Schwarz inequality as functions of $\Omega_{\mathrm{D1}}/\Gamma_{41}$. **(b)** The triphoton generation rates and the Cauchy–Schwarz inequality as functions of $\Omega_{\mathrm{D2}}/\Gamma_{51}$.

the system into the strong coupling regime between $|2\rangle$ and $|4\rangle$, while $\Omega_{\mathrm{D2}}$=0 MHz. The triphoton coincidence count displays damped Rabi oscillations along the $\tau_{21}$ direction, accompanied by exponential anti-bunching along $\tau_{31}$. The oscillatory behavior arises from quantum interference among multiple resonant channels [31]. In terms of the non-Hermitian eigenvalue structure, the eigenvalue $\delta_{\mathrm{D1}}$ possesses two real and one imaginary component ($\Omega_{\mathrm{D1}} > \Gamma_{diffa}$), characteristic of strong coupling, while $\delta_{\mathrm{D2}}$ remains in the weak regime. This scenario corresponds to region B in Fig. 1(e) and the energy-level structure depicted in Fig. 2(d), where dressed-state formation leads to a significant modification the triphoton correlation. These results demonstrate the ability to modulate triphoton temporal correlations through controlled variation of external control beams, offering a tunable platform to explore quantum interference, exceptional-point physics, and non-Hermitian dynamics in a multi-photon setting.

To further investigate the structure of the triphoton quantum state, we analyze the correlation characteristics of its two-photon subsystems by extracting conditional two-photon coincidence counts from the measured triphoton coincidence count. This is achieved by integrating the triphoton coincidence histogram along one temporal axis, yielding the conditional coincidences between photon pairs [38]. Specifically, the conditional two-photon coincidence counts as functions of $\tau_{21}$ (between $E_{S1}$ and $E_{S2}$) and $\tau_{31}$ (between $E_{S1}$ and $E_{S3}$) derived from Fig. 3(a) are shown in Figs. 3(a1) and (a2), respectively. In Fig. 3(a1), the $\tau_{21}$ distribution exhibits an anti-bunched exponential decay, indicating strong photon correlation between $E_{S1}$ and $E_{S2}$. By tracing out one photon from the triphoton state, partial entanglement persists in the remaining bipartite subsystem, manifesting as conditional two-photon correlations. This behavior aligns with the essential characteristics of the tripartite $W$ class [38]. Similarly, Fig. 3(a2) shows that the $\tau_{31}$ distribution also displays an anti-bunched exponential profile for the $E_{S1}$–$E_{S3}$ photon pair. As shown in Figs. 3(a1)–(c1), the conditional two-photon coincidence along the $\tau_{21}$ undergoes a distinct transition: starting with an anti-bunched exponential decay in Fig. 3(a1), transitioning to a single-exponential decay in Fig. 3(b1), and ultimately developing into damped Rabi oscillations in Fig. 3(c1). This progression reflects a continuous modulation of the coupling strength between energy levels $|2\rangle$ and $|4\rangle$, driven by the gradual enhancement of $\Omega_{\mathrm{D1}}$. In contrast, the $\tau_{31}$ correlations shown in Figs. 3(a2)–(c2) remain in the anti-bunched exponential decay, indicating that the coupling pathway responsible for $E_{S3}$ remains in a weak coupling regime throughout.

In Fig. 3(d), the Rabi frequency of $E_{\mathrm{D1}}$ and $E_{\mathrm{D2}}$ are $\Omega_{\mathrm{D1}} = 0$ MHz and $\Omega_{\mathrm{D2}} = 3.5$ MHz, respectively. The triphoton coincidence counting exhibits anti-bunch exponential decay in both the $\tau_{21}$ and $\tau_{31}$ directions. According to the system's eigenvalue analysis, $\delta_{\mathrm{D2}}$ corresponds to weak coupling regimes where $\Omega_{\mathrm{D2}} < \Gamma_{diffb}$, resulting in one real and two imaginary components. The associated energy-level configuration corresponds to Fig. 2(e), where both coupling pathways remain weak.

In Fig. 3(e), the triphoton coincidence data are collected with $\Omega_{\mathrm{D2}} = 26.4$ MHz. Compared with Fig. 3(d), the triphoton coincidence counts reveal a clear transition along the $\tau_{31}$ direction, evolving from anti-bunched to single-exponential decay, while the $\tau_{21}$ profile retains an anti-bunched exponential. According to eigenvalue analysis, in this regime $\Omega_{\mathrm{D2}} = \Gamma_{diffb}$ for $\delta_{\mathrm{D2}}$. This implies that the coupling between $|4\rangle$ and $|5\rangle$ has reached an exceptional point. The corresponding energy-level configuration is illustrated in Fig. 2(f). The conditional two-photon coincidences results shown in Figs. 3(e1) and (e2) further confirm this behavior: the $\tau_{21}$ curve displays an anti-bunched exponential decay, while the $\tau_{31}$ distribution exhibits a single-exponential decay.

Figure 3(f) presents triphoton coincidence counting acquired with $\Omega_{\mathrm{D2}} = 39.5$ MHz. Compared with Fig. 3(d), the triphoton coincidence counting exhibits damped Rabi oscillations in the $\tau_{31}$ direction, while maintaining an anti-bunching exponential decay in the $\tau_{21}$ direction. In this case, $\delta_{\mathrm{D2}}$ satisfies $\Omega_{\mathrm{D2}} > \Gamma_{diffb}$, indicating strong coupling between $|4\rangle$ and $|5\rangle$. This state corresponds to regime C in Fig. 1(e), with the associated energy-level diagram shown in Fig. 2(f). The conditional two-photon coincidence counting in the $\tau_{21}$ [Fig. 3(e1)] displays an anti-bunching exponential decay, while it exhibits damped Rabi oscillations in the $\tau_{31}$ [Fig. 3(e2)].

In addition to the correlation measurements discussed above, it is valuable to investigate the triphoton generation rate and the violation of the Cauchy–Schwarz inequality under varying coupling conditions, in order to gain further insight into the proposed generation mechanism. Figure 4 illustrates the normalized triphoton generation rates and the corresponding value of the Cauchy–Schwarz inequality, respectively, mapped as functions of the coupling strengths $\Omega_i/\Gamma_i$. Figure 4(a) shows the normalized triphoton generation rate and the value of the triphoton Cauchy–Schwarz inequality under various $\Omega_{\mathrm{D1}}/\Gamma_{41}$. The normalization is introduced to highlight the relative change induced by the non-Hermitian coupling strength. In the experiment, the reference value corresponding to the normalized rate of 1 represents 3380 detected triphoton events accumulated over one hour. The results clearly show that the generation rate and the value of the Cauchy–Schwarz inequality increase substantially as the $\Omega_{\mathrm{D1}}/\Gamma_{41}$ is enhanced. This behavior arises from the modulation of the effective coupling between atomic energy levels, which alters the number and structure of available resonant channels in the SSWM process.

Figure 4(b) presents the corresponding results as functions of $\Omega_{\mathrm{D2}}/\Gamma_{51}$. In this case, the reference value corresponding to the normalized rate of 1 represents 3456 detected triphoton events accumulated over one hour. With increasing $\Omega_{\mathrm{D2}}/\Gamma_{51}$, both the normalized triphoton generation rate and the degree of Cauchy–Schwarz inequality violation increase significantly. This trend further confirms that the SSWM process not only enables efficient triphoton generation but also facilitates access to strongly nonclassical quantum states through controlled energy-level coupling.

## 4 Conclusion

In this experiment, we have achieved the dynamical control of energy-level coupling states in the generation of *W*-state entangled triphotons via a spontaneous six-wave mixing (SSWM) process, enabled by two external control fields $E_{\mathrm{D1}}$ and $E_{\mathrm{D2}}$. By precisely tuning corresponding Rabi frequencies $\Omega_{\mathrm{D1}}$ and $\Omega_{\mathrm{D2}}$, we realized a dynamic modulation from the weak to the strong coupling regime in two independent energy-level subsystems. The measurements reveal that the coupling interactions in these subsystems can be selectively controlled, allowing one triphoton generation pathway to be strongly enhanced while the other remains in a weak-coupling regime. This feature enables the simultaneous realization of high generation efficiency and independently controllable correlation channels, providing enhanced flexibility for multiphoton quantum-state manipulation. This tunability was directly manifested in the triphoton coincidence distributions, which evolved from antibunching behavior to damped Rabi oscillations, confirming the presence of coherent multiphoton dynamics. Moreover, the emergence of single-exponential decay in the coincidence counting serves as a clear signature of exceptional points (EPs), linking non-Hermitian eigenvalue coalescence to observable multiphoton correlation dynamics. These results establish a direct correspondence between non-Hermitian coupling engineering and the reconfiguration of triphoton temporal correlations. Overall, this work provides a versatile platform for the coherent control of multiphoton quantum states through non-Hermitian light–matter interactions, opening new avenues for high-dimensional quantum state engineering, precision metrology, and the exploration of non-Hermitian quantum optics.

**Declarations** The authors declare no competing financial interest.

**Electronic supplementary materials** The online version contains supplementary material available at https://doi.org/10.15302/frontphys.2026.072203.

**Acknowledgements** This work was supported by the National Natural Science Foundation of China (Nos. 62475208, 62475209, and 12474392).

## References

1. R. El-Ganainy, K. G. Makris, M. Khajavikhan, Z. H. Musslimani, S. Rotter, and D. N. Christodoulides, Non-Hermitian physics and PT symmetry, *Nat. Phys.* 14(1), 11 (2018)
2. Z. Li, L. W. Wang, X. L. Wang, Z. K. Lin, G. Ma, and J. Jiang, Observation of dynamic non-Hermitian skin effects, *Nat. Commun.* 15(1), 6544 (2024)
3. Y. H. Lai, Y. K. Lu, M. G. Suh, Z. Q. Yuan, and K. Vahala, Observation of the exceptional-point-enhanced Sagnac effect, *Nature* 576(7785), 65 (2019)
4. S. Xia, D. Kaltsas, D. Song, I. Komis, J. Xu, A. Szameit, H. Buljan, K. G. Makris, and Z. Chen, Nonlinear tuning of PT symmetry and non-Hermitian topological states, *Science* 372(6537), 72 (2021)
5. I. Mandal and E. J. Bergholtz, Symmetry and higher-order exceptional points, *Phys. Rev. Lett.* 127(18), 186601 (2021)
6. H. Hodaei, A. U. Hassan, S. Wittek, H. Garcia-Gracia,

R. El-Ganainy, D. N. Christodoulides, and M. Khajavikhan, Enhanced sensitivity at higher-order exceptional points, *Nature* 548(7666), 187 (2017)

7. Ş. K. Özdemir, S. Rotter, F. Nori, and L. Yang, Parity–time symmetry and exceptional points in photonics, *Nat. Mater.* 18(8), 783 (2019)
8. T. Chen, W. Gou, D. Xie, T. Xiao, W. Yi, J. Jing, and B. Yan, Quantum zeno effects across a parity–time symmetry breaking transition in atomic momentum space, *npj Quantum Inf.* 7, 78 (2021)
9. B. Chen, Z. Zhao, and S. M. Morris, Chiral switches bring new twist to photonics, *Nat. Photonics* 16(3), 174 (2022)
10. Z. Zhang, D. Ma, J. Sheng, Y. Zhang, Y. Zhang, and M. Xiao, Non-Hermitian optics in atomic systems, *J. Phys. At. Mol. Opt. Phys.* 51(7), 072001 (2018)
11. L. Yang, M. Mao, C. Kong, and J. Liu, Nonreciprocal coupling modulated difference-sideband generation in a double-cavity optomechanical system, *Opt. Express* 31(21), 34560 (2023)
12. Q. Q. Zhu, Y. J. Fan, S. Z. Xiao, Y. B. Lou, S. S. Liu, and J. T. Jing, All-optical entanglement recovery in a correlated noisy channel, *Front. Phys. (Beijing)* 21(6), 062201 (2026)
13. C. Liang, Y. J. Tang, A. N. Xu, and Y. C. Liu, Observation of exceptional points in thermal atomic ensembles, *Phys. Rev. Lett.* 130(26), 263601 (2023)
14. J. S. Pan and F. Wu, Nonadiabatic transitions in non-Hermitian PT-symmetric two-level systems, *Phys. Rev. A* 109(2), 022245 (2024)
15. L. Ding, K. Shi, Q. Zhang, D. Shen, X. Zhang, and W. Zhang, Experimental determination of PT-symmetric exceptional points in a single trapped ion, *Phys. Rev. Lett.* 126(8), 083604 (2021)
16. Q. Zhong, J. Kou, Ş. K. Özdemir, and R. El-Ganainy, Hierarchical construction of higher-order exceptional points, *Phys. Rev. Lett.* 125(20), 203602 (2020)
17. F. Roccati, M. Bello, Z. Gong, M. Ueda, F. Ciccarello, A. Chenu, and A. Carollo, Hermitian and non-Hermitian topology from photon-mediated interactions, *Nat. Commun.* 15(1), 2400 (2024)
18. Y. Jiang, Y. F. Mei, Y. Zuo, Y. H. Zhai, J. Li, J. Wen, and S. Du, Anti-parity–time symmetric optical four-wave mixing in cold atoms, *Phys. Rev. Lett.* 123(19), 193604 (2019)
19. P. Kumar, S. Saravi, T. Pertsch, F. Setzpfandt, and A. A. Sukhorukov, Nonlinear quantum spectroscopy with parity–time-symmetric integrated circuits, *Photon. Res.* 10(7), 1763 (2022)
20. C. Hang and G. Huang, Parity–time symmetry with coherent atomic gases, *Adv. Phys. X* 2(3), 737 (2017)
21. Z. Lin, A. Pick, M. Lončar, and A. W. Rodriguez, Enhanced spontaneous emission at third-order Dirac exceptional points in inverse-designed photonic crystals, *Phys. Rev. Lett.* 117(10), 107402 (2016)
22. Z. K. Wu, K. G. Chang, Y. Hu, Y. Z. Zhang, Z. H. Jiang, and Y. P. Zhang, Modulation of four-wave mixing via photonic band gap, *Front. Phys. (Beijing)* 9(5), 665 (2014)
23. X. Ling, H. Zhao, X. Zhang, and J. Wu, Triphoton generation and heralded biphotons via spontaneous six-wave mixing in coherently driven cold atoms, *Phys. Rev. A* 112(1), 013706 (2025)
24. Z. G. Wang, P. Ying, P. Y. Li, H. Y. Lan, H. Q. Huang, H. Tian, J. P. Song, and Y. P. Zhang, Phase regulated suppression and enhancement switches of four-wave mixing and fluorescence, *Front. Phys. (Beijing)* 9(2), 153 (2014)
25. M. D. Lukin and A. Imamoğlu, Controlling photons using electromagnetically induced transparency, *Nature* 413(6853), 273 (2001)
26. S. Tagouegni, F. Fotsa-Ngaffo, and A. Kenfack-Jiotsa, Non-Hermitian electronics multipods of electromagnetically induced transparency (EIT) and absorption (EIA), *Opt. Quantum Electron.* 54(3), 200 (2022)
27. Y. Zheng, Z. Liu, J. Tang, J. Xu, C. Li, and G. Guo, Position-correlated biphoton wavefront sensing for quantum adaptive imaging, *Light Sci. Appl.* 14(1), 311 (2025)
28. Z. K. Wu, Y. Q. Zhang, T. K. Liu, Z. Y. Zhang, C. Li, Y. P. Zhang, and M. Xiao, Coherent control of dressed images of four-wave mixing, *Front. Phys. (Beijing)* 8(2), 228 (2013)
29. Y. Qian, L. Tang, D. Lai, and B. Hou, Enhanced asymmetric entanglement dynamics at higher-order exceptional points via optomechanical induced squeezing, *Phys. Rev. A* 112(4), 043548 (2025)
30. Q. Y. Chen, R. Zhuang, S. N. Liu, J. X. Wei, G. B. Liu, Z. Feng, and Y. P. Zhang, Three-mode quantum criteria of exceptional points in energy-level cascaded four-wave mixing, *J. Opt. Soc. Am. B* 42(9), 1891 (2025)
31. K. K. Li, Y. Cai, J. Yan, Z. Feng, F. Liu, L. Zhang, F. Li, and Y. Zhang, Direct manipulation of biphoton generation from the non-Hermitian nature of light–matter interaction, *Laser Photonics Rev.* 19(11), 2402149 (2025)
32. A. A. Zyablovsky, A. P. Vinogradov, A. A. Pukhov, A. V. Dorofeenko, and A. A. Lisyansky, PT-symmetry in optics, *Phys. Uspekhi* 57(11), 1063 (2014)
33. Z. Feng, S. Q. Zhang, R. Zhuang, G. B. Liu, F. Li, K. Li, and Y. Zhang, Backward time-correlated $W$-state triphoton generation via atomic coherence, *ACS Photonics* 12(8), 4305 (2025)
34. M. Eibl, N. Kiesel, M. Bourennane, C. Kurtsiefer, and H. Weinfurter, Experimental realization of a three-qubit entangled $W$ state, *Phys. Rev. Lett.* 92(7), 077901 (2004)
35. F. F. Du, M. Ma, X. M. Ren, and G. Fan, Entanglement concentration of $W$ state using linear optics with a higher success probability, *Quantum Inform. Process.* 23(4), 134 (2024)
36. C. Shu, P. Chen, T. K. A. Chow, L. B. Zhu, Y. Xiao, M. M. T. Loy, and S. Du, Subnatural-linewidth biphotons from a Doppler-broadened hot atomic vapour cell, *Nat. Commun.* 7(1), 12783 (2016)
37. K. K. Li, Y. Cai, J. Wu, Y. L. Liu, S. Q. Xiong, Y. Li, and Y. Zhang, Three-body topology entanglement generation via a six-wave mixing: Competing and coexisting of linear and nonlinear optics responses in triphoton temporal correlation, *Adv. Quantum Technol.* 3(5), 1900119 (2020)
38. K. K. Li, J. M. Wen, Y. Cai, S. V. Ghamsari, C. B. Li,

F. Li, Z. Zhang, Y. Zhang, and M. Xiao, Direct generation of time-energy-entangled $W$ triphotons in atomic vapor, *Sci. Adv.* 10(37), eado3199 (2024)

39. J. M. Wen, P. Xu, M. H. Rubin, and Y. Shih, Transverse correlations in triphoton entanglement: Geometrical and physical optics, *Phys. Rev. A* 76(2), 023828 (2007)
40. S. Q. Zhang, H. T. Tang, J. J. Wei, J. X. Wei, I. Ahmed, and Y. Zhang, One-step generation of energy-time-polarization-hyper-entangled $W$-class triphotons: Nonlinear and linear optical responses, *Ann. Phys.* 535(11), 2300208 (2023)
41. S. F. Li, Y. F. Li, S. Q. Xiong, Y. S. Qin, Y. Feng, Y. Zhao, X. Yu, and Y. Zhang, Coherent control of multi-photon using multidressing fields, *Ann. Phys.* 533(12), 2100083 (2021)
42. L. Xiao, X. Zhan, Z. H. Bian, K. K. Wang, X. Zhang, X. P. Wang, J. Li, K. Mochizuki, D. Kim, N. Kawakami, W. Yi, H. Obuse, B. C. Sanders, and P. Xue, Observation of topological edge states in parity–time-symmetric quantum walks, *Nat. Phys.* 13(11), 1117 (2017)
43. S. W. Du, J. M. Wen, M. H. Rubin, and G. Y. Yin, Four-wave mixing and biphoton generation in a two-level system, *Phys. Rev. Lett.* 98(5), 053601 (2007)